Artificial apposition compound eye fabricated by micro-optics technology

Jacques Duparré, Peter Dannberg, Peter Schreiber, Andreas Bräuer, and Andreas Tünnermann

By exploring micro-optical design principles and technology, we have developed an artificial apposition compound eye. The overall thickness of the imaging system is only 320 μm, the diagonal field of view is 21°, and the *f*-number is 2.6. The monolithic device consists of an UV-replicated microlens array upon a thin silica substrate with a pinhole array in a metal layer on the back side. The pitch of the pinholes differs from that of the lens array to provide individual viewing angle for each channel. Theoretical limitations of resolution and sensitivity are discussed as well as fabrication issues and compared with experimental results. A method to generate nontransparent walls between optical channels to prevent cross talk is proposed.

OCIS codes: 110.0110, 350.3950, 150.0150.

1. Introduction

For small invertebrates that have external skeletons, eyes are very expensive in terms weight and consumption of metabolic energy. If the budget is tight, Nature prefers to distribute the image-capturing function to a matrix that comprises some small eye sensors instead of using a single eye.

A natural apposition compound eye consists of an array of lenses, each with a small number of associated photoreceptors.[1,2] For simplicity, we want to assume only one photoreceptor per lenslet. Every lenslet focuses light from a small solid angle $\Delta\phi$ of object space onto a single photoreceptor (see Fig. 1). A lens–photoreceptor unit forms one optical channel and is referred to as an ommatidium. Apposition eyes have some hundreds to as many as tens of thousands of these ommatidia packed in nonuniform hexagonal arrays, which sample angular object space at interommatidial angle $\Delta\Phi$. The field of view (FOV) of such an imaging system is determined by the radius of curvature R and the size of the eye.

The acuity of natural compound eyes was examined in detail by many authors who work in the fields of physiology and optics.[3–6] It was found that apposition compound eyes provide low volume and a large FOV but at the price of low spatial resolution and sometimes low sensitivity compared with single-aperture eyes.[7,8] Apposition compound eyes in Nature, however, usually show an optical performance close to the diffraction limit.

Various technical approaches to designing compact vision systems have adopted the principle of small apposition compound eyes. A general examination of ways in which to use artificial compound eyes has been made.[9] Gradient-index lens arrays in front of pinhole arrays and photodiode arrays build up an artificial apposition compound eye.[10] Here a diverging lens is used to increase the overall FOV. The overall image reconstruction is explained by moire sampling. Different arrangements of gradient-index lenses and pinholes in the individual cells of the arrays permit scale-invariant processing. A difference in pitch leads to a factor of magnification that can also be interpreted as enlargement of the overall FOV.[11] A drawback of these systems is that the number of image points is equal to the number of ommatidia. A special detector geometry with large pitch and low fill factor has to be applied to achieve high resolution with the moire image reconstruction. In a system that uses a thin observation module by bound optics, each cell of the imager array has a matrix of photoreceptors that picks up all the information on the individual images. A backprojection

The authors are with the Fraunhofer-Institut für Angewandte Optik und Feinmechanik, Albert Einstein Strasse 7, D-07745 Jena, Germany. J. Duparré's e-mail address is jacques.duparre@iof.fraunhofer.de.

Received 23 December 2003; revised manuscript received 3 May 2004; accepted 17 May 2004.

0003-6935/04/224303-08$15.00/0

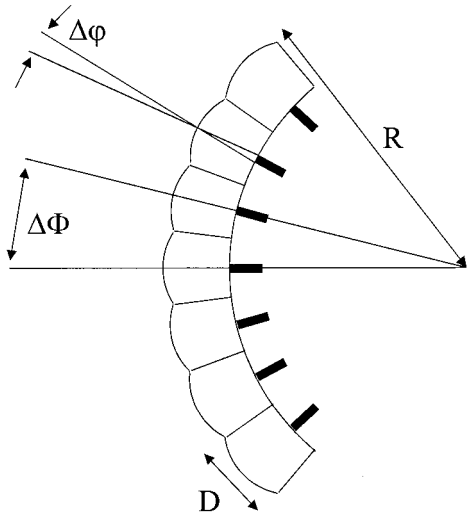

Fig. 1. Cross section of natural apposition compound eye with radius R and diameter of lenslets D. Interommatidial angle $\Delta\Phi$ and acceptance angles of the individual channels $\Delta\phi$ are shown.

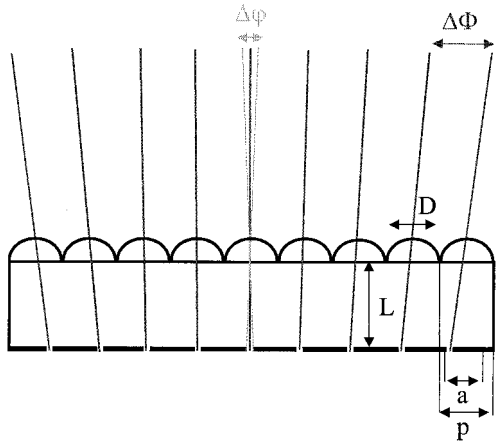

Fig. 2. Simplest setup of an artificial apposition compound eye. The optical axes and thus the directions of view of the ommatidia are directed outward owing to a difference in pitch Δp of microlens and pinhole arrays. The length of the objective is L; the pinhole array in a metal layer is located in the focal plane of the lens array. p, pitch of the optical channels; D, diameter of the lenslets. The size of each of the sampled microimages is a. $\Delta\Phi$ defines the angular sampling of the FOV and is known as the interommatidial angle. $\Delta\phi$ is the acceptance angle of an individual channel and is partly determined by pinhole diameter d. It is a measure of which solid angle in object space is represented by the optical system as one image point.

algorithm is used to retrieve the overall image from the many subimages.

To our knowledge, the technological approaches described so far suffer from assembly misalignment errors of the individually fabricated components. Because there are small required lens sags, artificial compound eyes are well suited for micro-optical fabrication technologies that permit wafer level manufacturing such as reflow process or polymer UV molding. Utilizing photolithography yields highly precise lateral accuracy. Fabrication and assembly technologies on a wafer scale lead to potentially cheap ultrathin imaging devices owing to parallel manufacturing of many systems at once.

In what follows, we discuss the design of an ultrathin monolithic vision system based on artificial compound eyes. The fabrication of the device is discussed, and experimental results for resolution and sensitivity are compared with simulation results.

2. Design and Simulations

An artificial apposition eye is constructed with a microlens array and a pinhole array in its focal plane (Fig. 2). The pinhole array can be replaced by an electronic detector array of equivalent geometry (pitch and active pixel size), or the pinhole array can be used to cover a detector array placed behind the substrate with larger pixels to achieve the desired resolution. Behind each microlens, a small subimage of the object is generated. Because there is a difference in pitch between the lens array and the pinhole array, a magnified moire image[13] is obtained. Each channel of this sampling camera corresponds to one field angle in object space with the optical axes of the channels directed outward (Fig. 2).

The angular resolution of artificial apposition compound eyes is defined by the interommatidial angle

$$\Delta\Phi = \arctan(\Delta p/f), \tag{1}$$

where Δp is the difference in pitch between microlens and pinhole arrays and f is the focal length of the lenslet, and by acceptance angle $\Delta\phi$ of the individual ommatidium, which is determined by the FWHM of the angular sensitivity function:

$$\Delta\phi = \arctan \frac{\mathrm{FWHM}(\hat{d} \otimes \mathrm{PSF})}{f}, \tag{2}$$

where PSF is the point-spread function of a lenslet, $\hat{d}$ stands for the transmittance distribution of a pinhole with diameter d, and $\otimes$ stands for convolution (following the Sparrow criterion[9]). We see that for a PSF that is large compared with the pinhole's diameter the acceptance angle is dominated by the pinhole only and that for a small PSF the pinhole's diameter has a minor influence on the acceptance angle. Assuming a Gaussian receptor acceptance function, a common approximation of Eq. (2) is[3]

$$\Delta\phi = \left[\left(\frac{d}{f}\right)^2 + \left(\frac{\lambda}{D}\right)^2\right]^{1/2}, \tag{3}$$

where D is the lens diameter and λ is the wavelength. This approximation will, however, give us a rough estimation for the circular aperture function as well. For good sensitivity of the device to a point source but also reasonable resolution, the size of the pinhole should approximately match the size of the PSF, which is given by the Airy-disk diameter

$$d_{\mathrm{Airy}} = 2.44\lambda f/D. \tag{4}$$

The maximum number of resolvable line pairs (LP) over the FOV is half the number of channels in the

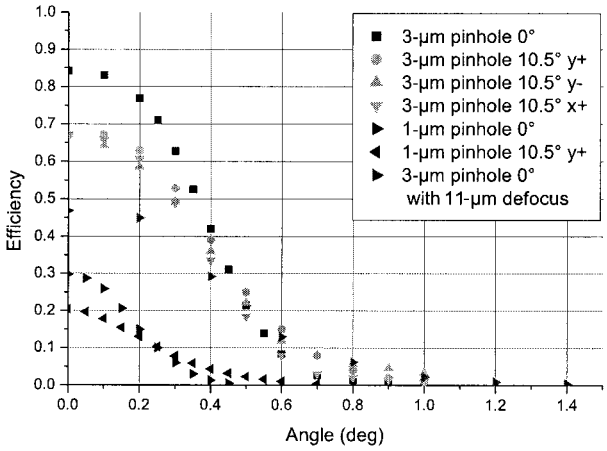

Fig. 3. Simulated angular sensitivity function for a single ommatidium with lens diameter 85 μm and 300-μm focal-length in glass. The sagittal ($x+$) and the tangential ($y\pm$) sensitivity functions are given; several pinholes sizes and field angles are examined. In the simulations the system is perfectly focused. One simulation, with 11-μm defocusing on axis with a 3-μm pinhole, is presented for comparison with experimental results. Free-space wave propagation was used between the lens and the pinhole to account for diffraction effects.

apposition eye if the acceptance angle of the individual ommatidia is perfectly matched to the interommatidial angle, which means that $\Delta\phi = 2\Delta\Phi$ (Nyquist criterion). If the acceptance angle of an individual ommatidium is large compared with the interommatidial angle, the period of resolvable LP is determined by the acceptance angle.

The FOV of the artificial apposition eye is given by

$$\mathrm{FOV} = \arctan(a/f), \tag{5}$$

where a is the size of one subimage. We chose $a < p$ to maintain some free space between the subimages to reduce cross talk and to be able in the future to apply opaque walls, as we described below. When $a = p$ the FOV is determined by the numerical aperture (NA) of the lenslets. The pitch difference of the pinhole array and the lens array for a camera with N channels along one dimension is calculated from

$$\Delta p = a\left(1 - \frac{N}{N+1}\right). \tag{6}$$

The FOV is independent of the number of channels. Because of the small focal length of the lenslets, a large depth of field is achieved.

The angular sensitivity function is commonly used to characterize the performance of a single ommatidium. Its FWHM gives acceptance angle $\Delta\phi$ from Eq. (2). The angular sensitivity function determines which solid angle in object space is treated by the optical system as one image point by plotting the efficiency of light from an object point received by a photoreceptor as a function of angular distance of the object point from the optical axis of the ommatidium considered. Figure 3 shows a simulation of a single ommatidium for which the efficiency is normalized to the flux incident upon the lens. We see that the apposition eye shows a clear trade-off between sensitivity and resolution: The larger the pinhole diameter, the larger the sensitivity but the worse the resolution and vice versa. As presented in Fig. 3, off-axis aberrations of the outer channels lead to larger spot sizes of image points for larger field angles and, thus, to wider and lower angular sensitivity functions, which are equivalent to lower angular resolution and lower sensitivity. An adaption of the pinhole size to the field angle would reduce the degradation of sensitivity with increasing field angle but further degrade the angular resolution in these cases.

The advantages of the artificial apposition eye could emerge in particular when the eye is used in connection with electronic vision sensors with high dynamic range contrast and large pixel pitch with a low fill factor.[14] The resolution properties of a compound eye imaging system can now be understood. In the next paragraph we analyze its interrelationship with sensitivity.

The sensitivity of a single-aperture imaging system to an extended source is determined by the system's f-number ($F/\#$).[15] This is so also for apposition compound eyes.[5] For a distant object the sensitivity is described by[16]

$$I_I = \frac{\pi\tau L_O}{4(F/\#)^2}, \tag{7}$$

where I_I is the irradiance in the image plane, τ is the transmission of the optical system, L_O is the radiance in the object plane, and $F/\# = f/D$. If the object scene is a perfect Lambertian radiator, L_O is constant over the hemispherical solid angle and it follows that $I_O = \pi L_O$, where I_O is the irradiance on the object's surface.[15] Sensitivity as the ratio of image to object irradiance can thus be simply expressed by

$$\frac{I_I}{I_O} = \frac{\tau}{4(F/\#)^2} = \tau\mathrm{NA}^2, \tag{8}$$

where $\mathrm{NA} \approx 1/2(F/\#)$ is the NA of the lenslet. To calculate the total flux that an individual receptor receives, one has to take into account the area of the receptor. Let P_I be the power in one pinhole; it follows that

$$P_I = \tau I_O \mathrm{NA}^2(\pi d^2/4). \tag{9}$$

Equation (9) is expanded by L^2/L^2, where L is the optical system's length, which is $L = f[1 + (n-1)/n]$, where n is the refractive index of the substrate ($n \approx 1.5$). Applying Eq. (3) with the pinhole diameter in a region much larger than the Airy disk's diameter and matching the diameter of the Airy disk such that $\Delta\phi \approx \sqrt{2}\, d/f$, we find that

$$P_I = \frac{9\pi}{128}\,\tau I_O \mathrm{NA}^2 L^2\,\frac{1}{1/(\Delta\phi^2)} \tag{10}$$

where $1/\Delta\phi^2$ is the resolution in LP/rad.

We can see that the sensitivity P_I/I_O is inversely

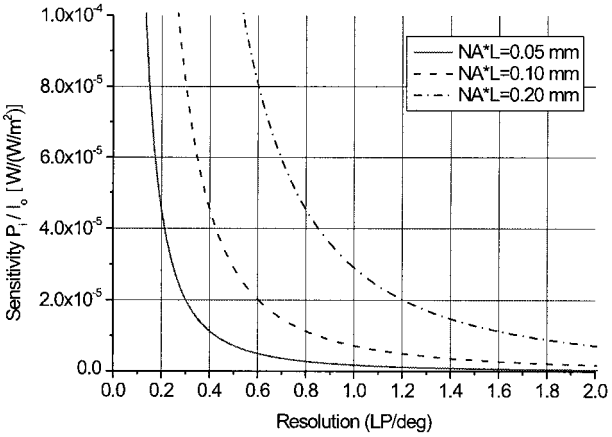

Fig. 4. Resolution of artificial compound eyes versus sensitivity to an extended source. For a given set of NA and system length there is a trade-off between sensitivity and resolution that is determined mainly by pinhole diameter d.

proportional to the square of the resolution with the squared product of the NA of the lenslets and the system length as the parameter. Figure 4 gives a representation of Eq. (10), assuming that $\tau = 1$.

This relation (as shown in Fig. 4) points out the main trade-off of artificial compound eyes. For a given set of parameters of NA and L, resolution and sensitivity cannot be increased at the same time. The overall performance of the eye can be improved only if the product NA L is increased.

3. Fabrication

Fabrication of the artificial apposition compound eye was carried out by lithography on a wafer scale, based on the patterning of a thin, 4-in. (10.16-cm) glass wafer with pinhole arrays on one side and microlens arrays on the opposite side. The thickness of the wafer is matched to the microlenses focal length in the glass. The pitch of the pinholes differs from that of the microlens arrays to produce an individual viewing angle of each channel. The parameters of different arrays on the pinhole photomask (array size, pinhole pitch, and diameter) were varied in such a way that different camera chips were obtained on each wafer. The pinholes (diameters, 1–6 μm) were generated by photolithography and wet etching of a 200-nm-thick metal film upon the glass wafer. The ideal diameter of the pinholes to capture as much light as possible at optimum resolution is expected to be $d \approx 3.5$ μm, from Eq. (4) with the system parameters given in Table 1 and assuming that $\lambda = 550$ nm. The generation of the microlens arrays consists of several steps involving master and mold generation and subsequent UV replication.[17] The photoresist's master pattern is fabricated upon a silicon wafer by a standard procedure (photolithography in combination with a heating–reflow process). The replication is carried out in a modified contact mask aligner (SUSS MA6 with UV embossing option) in which the gap between glass wafer and mask–mold is filled by an UV-curing inorganic–organic hybrid polymer that is subsequently cured and separated from the mold. The mask aligner facilitates compensation for wedge error as well as lateral and axial alignment of front and back side patterns. The most critical fabrication issue is uniformity of the axial distance between lens vertex and pinhole, which is affected by a series of parameters such as precision of the MA6 mask aligner's z axis (±1 μm), bowing of the mold, mask holder, chuck, and substrate (±3 μm overall), and by nonuniform microlens focal lengths across the wafer (±3 μm). The major technological parameters of the fabricated systems are compiled in Table 1.

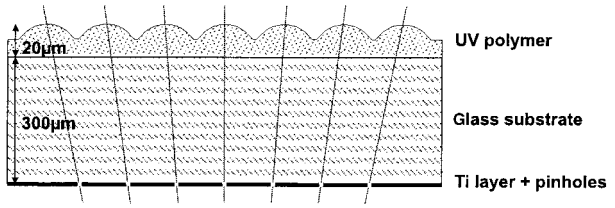

Fig. 5. Schematic side view of the fabricated artificial compound eye consisting of a lens array layer, a substrate, and a metal layer.

Figure 5 presents a schematic side view of the fabricated artificial compound eye; Fig. 6, a photograph of the front view. The lens array fills the whole substrate with identical lenses. The metal layer with

Table 1. Parameters of Fabricated Artificial Apposition Eye Wafers

Property	Parameter	Remark (Generated by)
Metal layer	Thickness, 200 nm	Titanium (sputtering)
Pinholes	Diameter, 1–6 μm	(Photolithography + wet etching)
Glass substrate	$d = 300 \pm 1$ μm	D263T 4-in. wafer
Replicated microlenses	Layer thickness, 20 μm	(UV molding)
UV polymer	Acrylate type, $n = 1.50$	Inorganic-organic hybrid polymer
Lens model	$R_c = 118$ μm; pitch 90 μm; diameter, 85 μm; sag, 10 μm	(Lithography and reflow)
Form deviation	<20 nm rms	
Size of sampled image	60 μm × 60 μm	Gap left to reduce cross talk
Lateral registration error	±3 μm	(Back side alignment in SUSS Microtec MA6)
Axial alignment–nonuniformity	±6 μm across 4 in.	Including focal-length nonuniformity
Array sizes	11 × 11–101 × 101	Each with a different pinhole size
Field of view	21°	On diagonal

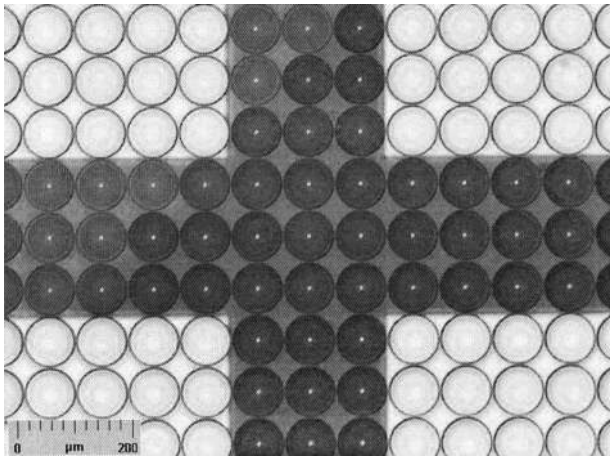

Fig. 6. Photograph of the front view of a demonstration wafer in the corner of a junction of four different cameras. The overlap of the metal layer and the lens array layer is presented to show the precision of replication. The lens array fills the whole substrate with identical lenses. The metal layer with the pinholes determines camera size, channel number, and increment of viewing direction of the individual cameras.

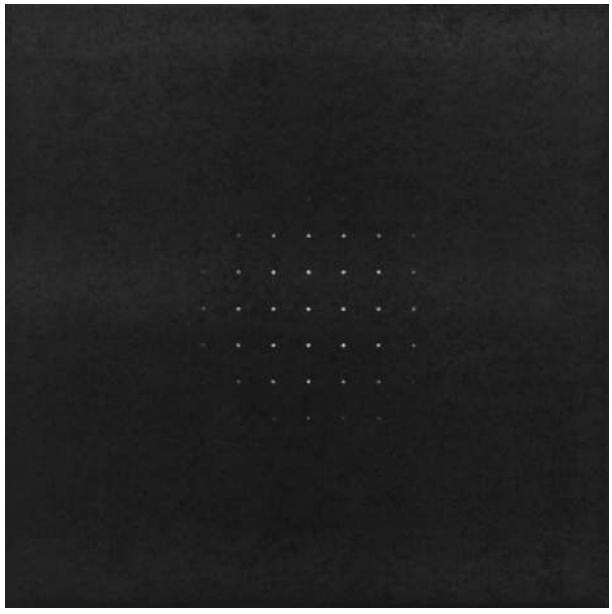

Fig. 7. Response to a point source: Image of the single-mode fiber end face obtained with a camera with 51 × 51 optical channels and 3-μm pinhole diameter. The separation of viewing directions of the individual channels is 0.3°. The response of several ommatidia in the camera to one source point gives an idea of the possible resolution of the device.

the pinholes determines separation, size, channel number, and increment of viewing direction of the individual cameras. For this first demonstrator no apertures were applied to the lens array layer to prevent stray light from coming through gaps between the lenses. The next technological steps will include application of such apertures.

4. Experimental Results

For characterization of the prototype, on the one hand we registered images of different bar targets with the pinhole array surface imaged onto a CCD and measured the contrast transfer function (CTF). To prevent cross talk between adjacent channels without optical isolation we matched the size of the test images presented to the device exactly to the device's FOV. On the other hand, the angular sensitivity function was determined for a single-mode fiber end face at a wavelength of 637 nm acting as point source. For measurement of the angular sensitivity function the fiber end face was moved laterally in object space at a distance of 300 mm in front of a single ommatidium while the power in the pinhole was determined. Additionally, images of the point source taken with a camera with a 51 × 51 channel were analyzed. The power measured in the pinhole was normalized to the total integrated power of one channel. The modulation transfer function (MTF) of the device was calculated from the measured angular acceptance function.

Figures 7 and 8 present the measured on-axis sensitivity function for a 3-μm pinhole. The measured angular sensitivity function has a FWHM of 1.5°, which is almost twice as large as we would have expected from the simulations as presented in Fig. 3. Accordingly, the experimental efficiency is much lower. Simulations showed that the experimentally achieved results correspond to 11-μm defocusing of the pinhole layer with respect to the lens array layer (Fig. 3). The reason for this deviation was found to be a discrepancy in the refractive index of the substrate material in design simulation and experimental achievement. It is thus not caused by the fabrication tolerances and will not be repeated in future fabrications. From the theoretical sensitivity

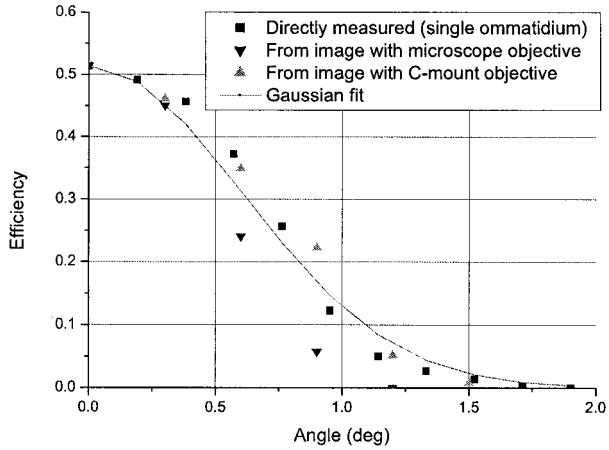

Fig. 8. Measured on-axis angular sensitivity function for ommatidia with lens diameter 85 μm and 300-μm focal length in glass. Pinhole diameter, 3 μm. Results of direct measurement for a single ommatidium while the point source was moved in front of it are presented. Additionally measured and normalized energies in images taken with a 51 × 51 channel camera for a point source and relayed with a microscope objective and a C-mount objective, respectively, on a CCD camera were analyzed. A Gaussian fit to the curves was made to quantify the curve shape.

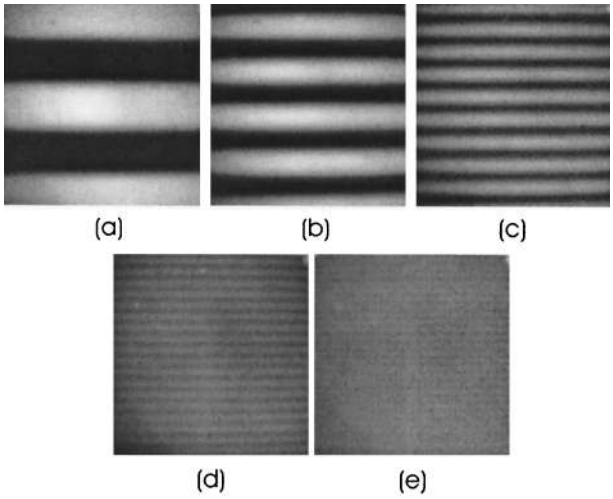

Fig. 9. Bar targets of different frequencies (in LPs/FOV) imaged by apposition-eye cameras with 101 × 101 channels, 15° horizontal FOV, and 3-μm pinhole diameter and relayed by a short working distance C-mount objective onto a CCD: (a) 2.5 LP/FOV, (b) 5 LP/FOV, (c) 10 LP/FOV, (c) 20 LP/FOV, (c) 28 LP/FOV. Image processing as Gaussian blurring (2 CCD pixels), brightness, contrast, and intensity were applied to enhance image quality, as done also by commercial digital cameras.

function in Fig. 3 (FWHM, 0.75°) we would expect that over the horizontal and vertical FOV of 15° at least 20 LP should be resolvable, so a sampling with 51 × 51 channels would gather all available information.

In Fig. 8 a Gaussian fit to the measured angular sensitivity functions with

$$f(x) = f_{\max} \exp\left(-\frac{x^2}{\sigma^2}\right), \tag{11}$$

where f is the efficiency as a function of the direction of view x, $f_{\max}$ is the maximum efficiency on axis, and σ is the e^{-1} width of the function, was made. A value of $\sigma = 0.85°$ resulted. Performing the Fourier transformation of the angular sensitivity function allows the MTF of an optical system to be calculated.[4,9] The MTF is thus given by

$$\mathrm{MTF}(\tilde{x}) = \exp\left(-2\pi \frac{\tilde{x}^2\sigma^2}{4\mathrm{FOV}^2}\right), \tag{12}$$

where FOV is the horizontal FOV of the camera and $\tilde{x}$ is the resolution in LP/horizontal FOV.

We measured the CTF of an apposition-eye camera with 101 × 101 channels, a 15° horizontal FOV, and 3-μm pinhole diameter imaging bar targets with different frequencies (Fig. 9). The CTF is defined as

$$\mathrm{CTF}(\tilde{x}) = \frac{I_{\max} - I_{\min}}{I_{\max} + I_{\min}}, \tag{13}$$

where $I_{\max}$ and $I_{\min}$ are the maximum and minimum intensities, respectively, of an imaged test target of frequency $\tilde{x}$.

If the image degradation is so large that an imaged bar target is represented by a sinusoidal image, one can calculate the equivalent MTF from the CTF by dividing the values of contrast by $\pi/4$ (Ref. 18; the first harmonic of the original bar target is taken as a reference). However, if the imaged bar targets are still well represented by rectangular functions, the MTF is equivalent to the CTF.

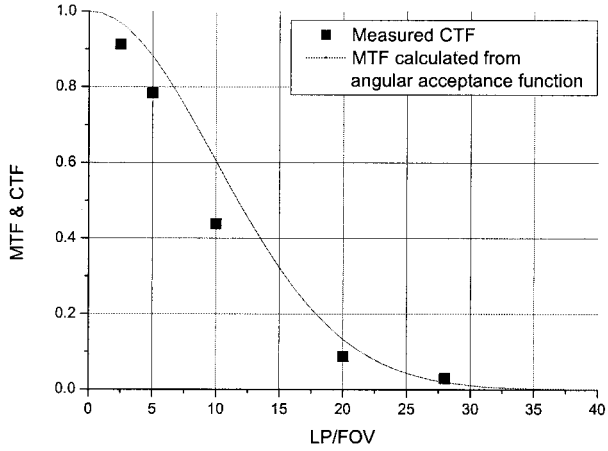

Fig. 10. Calculated MTF and measured CTF. The MTF was calculated from Eq. (12) with $\sigma = 0.85°$. The CTF was measured for the imaged bar targets presented above but acquired without any subsequent image processing except Gaussian blurring with 2 CCD pixels for smoothing of the images determined by the CCD resolution. For reasons of simplicity and unambiguousness over the progression of the curve the CTF is opposed to the MTF.

In Fig. 10 the calculated MTF and the measured CTF are compared. Within measurement and curve-fitting errors, good correspondence can be observed.

It can be seen from Fig. 10 that the cutoff of the MTF calculated from experimental data is above 30 LP/FOV. This is much larger than expected from the original angular sensitivity function and the determined amount of defocusing. The measured CTF is considerably lower, but still the cutoff is much larger than expected. The criterion of how many angular sensitivity functions fit into the field of view

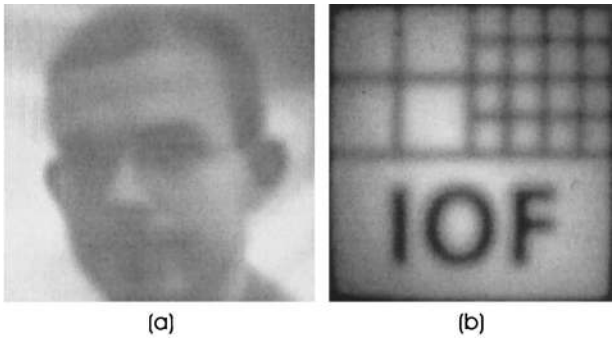

Fig. 11. Test patterns imaged by the same apposition-eye cameras as in Fig. 9. (a) Image of a passport photograph of J. Duparré. (b) Image of the Fraunhofer-Institut für Angewandte Optik und Feinmechanik logo. Test objects fill the FOV of the camera under test. Object distance has no noticeable influence on image quality.

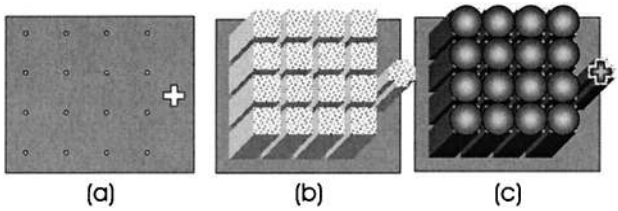

Fig. 12. Layout of a monolithic artificial apposition eye with optical isolation of the individual channels. Fabrication steps: (a) pinhole array upon a substrate, which works only as a carrier and can later be replaced by the electronics chip. (b) SU8 photopolymer pedestals with correct height structured on top. (c) Spaces between pedestals are filled with an absorbing polymer, and a microlens array, aligned to the pinholes, is embossed on the top in an UV-curing polymer.

seems to be much harder than a directly measured CTF. Obviously there is a also large degree of freedom to fit the Gaussian to the measured angular sensitivity curves, which results in a certain degree of freedom for the MTF.

Figure 11 presents two test images taken by cameras with 101 × 101 channels and 3-μm pinhole diameter and relayed by a short working distance C-mount objective onto a CCD.

The observable distortion and reduced illumination at the outer parts of the images are due mainly to the relay optics. Images with a high information content can obviously be transferred by the artificial apposition compound eye presented here. The number of resolvable pixels is sufficient for face recognition.

5. Conclusions and Outlook

We have presented a micro-optically fabricated artificial apposition compound eye imaging system with a thickness of 320 μm. It consists of a lens array and a pinhole array with different pitches in its focal plane and the optical axes of the ommatidia directed outward. Experimental and simulation results for angular sensitivity functions were presented, as well as images acquired with our first prototype of an artificial apposition compound eye. The contrast transfer function was experimentally determined and compared with the modulation transfer function calculated from the measured angular sensitivity function. The device showed a considerable amount of defocus, which decreased sensitivity and resolution. The reason for this deviation was determined and will not be repeated in future fabrication runs. Nevertheless, the experimentally determined cutoff of resolution is approximately at 30 line pairs over a horizontal field of view of 15°, which is sufficient for many sensor and imaging applications in which a small system thickness is emphasized.

It was proved that artificial compound eyes have the capability of drastically reducing imaging system length far below 1 mm. However, there is a trade-off among field of view, resolution, and sensitivity.

The factors that limit resolution of the fabricated artificial compound eye are the size of the solid angle in object space that each channel interprets as one image point and the relatively small field of view. The largest resolvable spatial frequency with the ultrathin objective described here is thus much smaller than the Nyquist frequency, which is determined by half the number of optical channels sampling the FOV.

When there are large angles of incidence from object points outside the FOV in the current setup, light focused by one lenslet may be received by a receptor of the adjacent channel. Ghost images from objects outside the FOV and a reduction of contrast may result. Nature solves this problem by introducing nontransparent walls between the ommatidia. To investigate the possibility of fabrication of a technical equivalent of those opaque walls and the influence on cross talk between channels, we are currently fabricating imaging chips by using a modification of the technology (Fig. 12). Here, light-protection walls will shield the various channels, leading to reduced cross talk. The region between pinholes and microlenses is formed by a patterned spacer layer (thickness, ~300 μm) consisting of transparent cones of SU8 photopolymer[19,20] (Epoxy-Novolak EPON SU8) and gaps that are filled by absorbing polymer cast. High aspect ratio SU8 features are fabricated by use of an additional photomask. Pinhole and microlens fabrication remains unchanged.

This study was partly funded by the European Commission project IST-2001-34646, WALORI (WAfer Level Optic solution for compact CMOS Imager).

References

1. R. Völkel, M. Eisner, and K. J. Weible, "Miniaturized imaging systems," Microelectron. Eng. **67–68,** 461–472 (2003).
2. R. Völkel, M. Eisner, and K. J. Weible, "Miniaturized imaging systems," presented at the Micro- and Nanoengineering International Conference, Lugano, Switzerland, 16–19 September 2002.
3. G. A. Horridge, "The compound eye of insects," Sci. Am. **237,** 108–120 (1977).
4. A. W. Snyder, "Acuity of compound eyes: physical limitations and design," J. Comp. Physiol. A **116,** 161–182 (1977).
5. K. Kirschfeld, "The absolute sensitivity of lens and compound eyes," Z. Naturforsch. **29,** 592–596 (1974).
6. R. Wehner, "Spatial vision in arthropods," in *Comparative Physiology and Evolution of Vision in Invertebrates—Handbook of Sensory Physiology*, H. Autrum, ed. (Springer-Verlag, Berlin, 1981), Vol. VII/6C, Chap. 4, pp. 287–317.
7. M. F. Land, "Variations in structure and design of compound eyes," in *Facets of Vision*, D. G. Stavenga and R. C. Hardie, eds. (Springer-Verlag, Berlin, 1989), Chap. 5, pp. 90–111.
8. G. A. Horridge, "Apposition eyes of large diurnal insects as organs adapted to seeing," Proc. R. Soc. London Ser. B **207,** 287–309 (1980).
9. J. S. Sanders and C. E. Halford, "Design and analysis of apposition compound eye optical sensors," Opt. Eng. **34,** 222–235 (1995).
10. K. Hamanaka and H. Koshi, "An artificial compound eye using a microlens array and its application to scale-invariant processing," Opt. Rev. **3,** 264–268 (1996).
11. S. Ogata, J. Ishida, and T. Sasano, "Optical sensor array in an artificial compound eye," Opt. Eng. **33,** 3649–3655 (1994).

12. J. Tanida, T. Kumagai, K. Yamada, S. Miyatake, K. Ishida, T. Morimoto, N. Kondou, D. Miyazaki, and Y. Ichioka, "Thin observation module by bound optics (TOMBO) concept and experimental verification," Appl. Opt. **40,** 1806–1813 (2001).
13. H. Kamal, R. Völkel, and J. Alda, "Properties of moiré magnifiers," Opt. Eng. **37,** 3007–3014 (1998).
14. P.-F. Rüedi, P. Heim, F. Kaess, E. Grenet, F. Heitger, P.-Y. Burgi, S. Gyger, and P. Nussbaum, "A 128 × 128 pixel 120 dB dynamic range vision sensor chip for image contrast and orientation extraction," in *IEEE International Solid-State Circuits Conference* (Institute of Electrical and Electronics Engineers, Piscataway, N.J., 2003), paper 12.8.
15. R. McCluney, *Introduction to Radiometry and Photometry* (Artech House, Boston, Mass., 1994).
16. R. Kingslake, *Optical System Design* (Academic, London, 1983).
17. P. Dannberg, G. Mann, L. Wagner, and A. Bräuer, "Polymer UV-molding for micro-optical systems and O/E-integration," in *Micromachining for Micro-Optics*, S. H. Lee and E. G. Johnson, eds., Proc. SPIE **4179,** page 137 ff. SPIE, 2000.
18. H. Naumann and G. Schröder, *Bauelemente der Optik—Taschenbuch der technischen Optik*, 6th ed. (Hanser-Verlag, Munich, 1992).
19. M. Shaw, D. Nawrocki, R. Hurditch, and D. Johnson, "Improving the process capability of SU-8," Microsystems Technologies **10,** 1–6 (2003).
20. R. Rumpf and E. Johnson, "Micro-photonic systems utilizing SU-8," in *MOEMS and Miniaturized Systems IV*, A. El-Fatatry, ed., Proc. SPIE **5346,** 64–72 (2004).